Article

Neuron

Precision of Inhibition: Dendritic Inhibition by Individual GABAergic Synapses on Hippocampal Pyramidal Cells Is Confined in Space and Time

Highlights

- New paradigm to measure inhibition by individual GABAergic synapses
- A realistic model for dendritic Ca^{2+} inhibition
- Ca^{2+} transients from back-propagating APs are inhibited with large dynamic range
- Ca^{2+} is inhibited with micrometer/millisecond precision in both shafts and spines

Authors

Fiona E. Müllner, Corette J. Wierenga, Tobias Bonhoeffer

Correspondence

muellner@neuro.mpg.de

In Brief

By imaging action potential-evoked dendritic calcium signals and simultaneously activating identified inhibitory synapses, Müllner et al. measured the spatio-temporal profile of inhibition exerted by individual GABAergic synapses, which fills a gap in the biophysical understanding of dendritic inhibition.

Müllner et al., 2015, Neuron *87*, 576–589
August 5, 2015
http://dx.doi.org/10.1016/j.neuron.2015.07.003

CellPress

CellPress

Neuron
Article

Precision of Inhibition: Dendritic Inhibition by Individual GABAergic Synapses on Hippocampal Pyramidal Cells Is Confined in Space and Time

Fiona E. Müllner,[1,2,*] Corette J. Wierenga,[1,3,4] and Tobias Bonhoeffer[1,4]
[1]Max Planck Institute of Neurobiology, Synapses - Circuits - Plasticity, 82152 München-Martinsried, Germany
[2]Present address: Neural Circuit Laboratories, Friedrich Miescher Institute for Biomedical Research, 4058 Basel, Switzerland
[3]Present address: Faculty of Science, Utrecht University, 3584 CH Utrecht, Netherlands
[4]Co-senior author
*Correspondence: muellner@neuro.mpg.de
http://dx.doi.org/10.1016/j.neuron.2015.07.003

SUMMARY

Inhibition plays a fundamental role in controlling neuronal activity in the brain. While perisomatic inhibition has been studied in detail, the majority of inhibitory synapses are found on dendritic shafts and are less well characterized. Here, we combine paired patch-clamp recordings and two-photon Ca^{2+} imaging to quantify inhibition exerted by individual GABAergic contacts on hippocampal pyramidal cell dendrites. We observed that Ca^{2+} transients from back-propagating action potentials were significantly reduced during simultaneous activation of individual nearby inhibitory contacts. The inhibition of Ca^{2+} transients depended on the precise spike-timing (time constant < 5 ms) and declined steeply in the proximal and distal direction (length constants 23–28 μm). Notably, Ca^{2+} amplitudes in spines were inhibited to the same degree as in the shaft. Given the known anatomical distribution of inhibitory synapses, our data suggest that the collective inhibitory input to a pyramidal cell is sufficient to control Ca^{2+} levels across the entire dendritic arbor with micrometer and millisecond precision.

INTRODUCTION

The coordinated action of excitation and inhibition is at the basis of several fundamental aspects of neuronal processing, including network oscillations (Mann and Paulsen, 2007), tuning to sensory stimuli (Shapley et al., 2003), and plasticity of neuronal circuits (Baroncelli et al., 2011). Inhibition in the CNS is exerted by perisomatically and dendritically targeting interneurons which can perform different inhibitory tasks (Miles et al., 1996; Royer et al., 2012). In general, perisomatically targeting GABAergic interneurons are well understood in terms of their capability to control spike timing and network oscillations (Cobb et al., 1995; Pouille and Scanziani, 2001). Inhibition by dendritic inhibitory synapses, however, is understood to a much lesser degree, as the limited accessibility of small dendritic compartments has impeded experimental approaches. For lack of biological data, the question how individual inhibitory inputs are integrated by dendrites has fueled decades of theoretical literature. Since the 1970s, computational studies have explored how inhibitory synapses should be optimally placed to inhibit excitatory postsynaptic potentials (EPSPs) (Jack et al., 1975; Koch et al., 1983; Segev and Parnas, 1983) and also, more recently, how dendritic inhibition interferes with active dendritic conductances such as Ca^{2+} spikes (Gidon and Segev, 2012; Jadi et al., 2012) or I_h currents (Park and Kwag, 2012) to control spike threshold or spike timing of the postsynaptic cell. On these grounds, multi-compartmental modeling has predicted that inhibition of dendritic Ca^{2+} transients should modulate synaptic plasticity like long-term potentiation or depression (LTP/LTD, see Cutsuridis, 2011; Bar-Ilan et al., 2012).

Experimentally, the function of dendritic inhibition has been explored mainly on the cellular and not so much on the subcellular scale. By interfering with Ca^{2+}-dependent processes by pharmacology and multi-synaptic stimulation (Meredith et al., 2003; Tsukada et al., 2005; Nishiyama et al., 2010; Groen et al., 2014), $GABA_A$-receptor-mediated dendritic inhibition has been shown to modulate spike-timing-dependent plasticity rules—sometimes even converting LTP-inducing into LTD-inducing stimuli. Addressing inhibition of Ca^{2+} processes more directly, a number of elegant studies have described dendritic inhibition of Ca^{2+}-dependent spikes upon activation of single (Larkum et al., 1999) or multiple (Miles et al., 1996; Tsubokawa and Ross, 1996) dendrite-targeting inhibitory interneurons in brain slices, as well as in vivo (Murayama et al., 2009). On top of $GABA_A$-dependent effects, some of this inhibition is also mediated by $GABA_B$ receptor activation (Pérez-Garci et al., 2006, 2013; Chalifoux and Carter, 2011; Breton and Stuart, 2012). On a population level, dendritic inhibition acts as a key regulator of neuronal input-output transformations (Lovett-Barron et al., 2012; Müller et al., 2012).

On the subcellular scale, experimental data elucidating the function of dendritic inhibition have so far been restricted to paradigms with limited spatial and temporal resolution. Studies using GABA and glutamate iontophoresis have shown that activation of $GABA_A$ receptors interferes with glutamatergic inputs if they are located on the same dendritic branch (Liu, 2004;

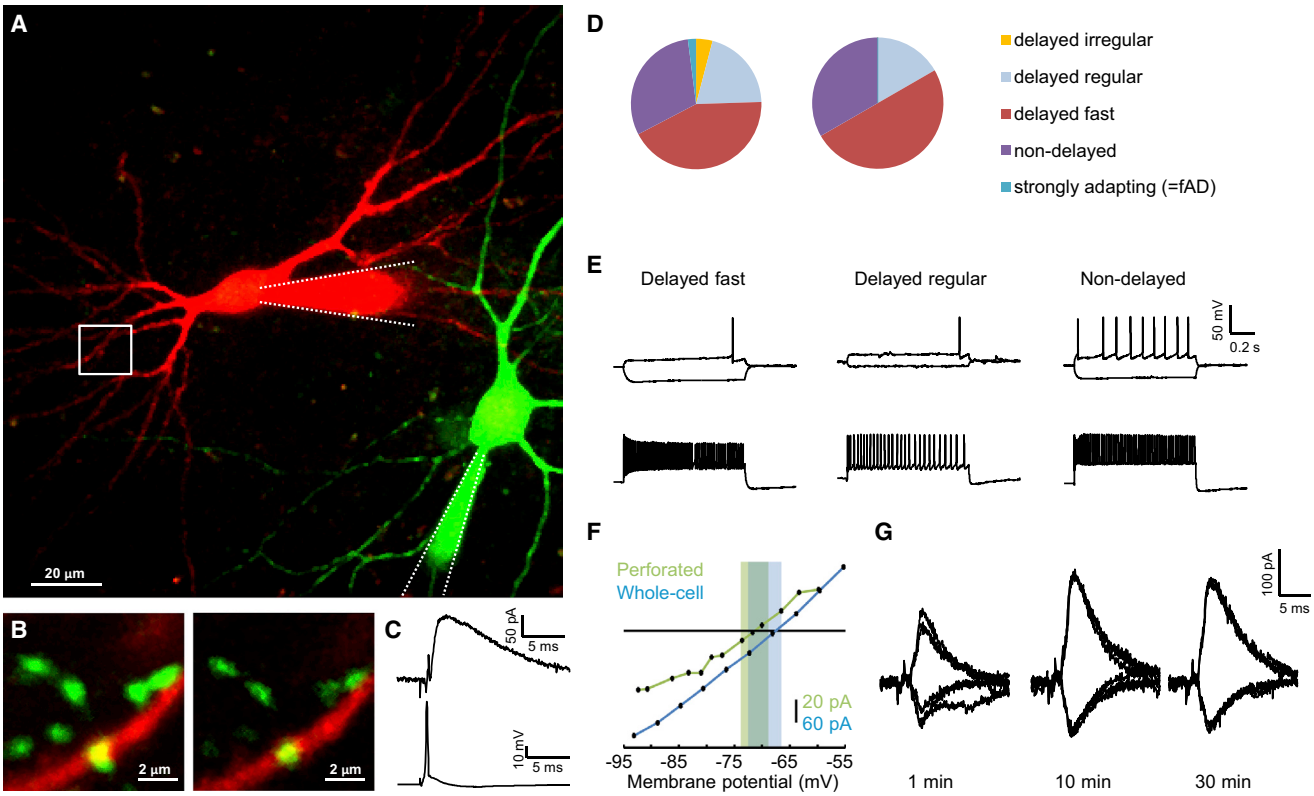

Figure 1. Recording Configuration

(A) GAD65-GFP-positive interneuron (200 µM Alexa 488 filled, green) and pyramidal cell (30 µM Alexa 594 and 200 µM Fluo5F filled, red). Dotted lines contour patch pipettes.

(B) Zoom-in to boxed area in (A): morphological contact between the axon (green) and dendrite (red) indicates a putative inhibitory synapse (2PLSM image, left: maximum projection, right: single z plane).

(C) IPSC recorded in the pyramidal cell voltage clamped at −40 mV (top), following an AP in the inhibitory interneuron (bottom).

(D) Electrophysiological classification of selected GABAergic interneurons. Left: connected INs (n = 49); right: subset of INs included in our dataset (n = 12), excluding, e.g., cells with no contacts detected or with IPSC rundown.

(E) Representative firing pattern of the three groups delayed fast/delayed regular/non-delayed (Wierenga et al., 2010).

(F) Representative IV curves for perforated-patch and whole-cell recordings. The overlapping blue and green bars represent the respective 95% confidence intervals of mean reversal potential at 24°C.

(G) IPSCs recorded at alternating −40 and −100 mV holding potentials to track stability of the reversal potentials during whole-cell (see Figure S1 for summary data). Time in whole-cell annotated.

Hao et al., 2009). Likewise, one-photon GABA uncaging locally interferes with Ca^{2+} transients from back-propagating action potentials (Lowe, 2002; Kanemoto et al., 2011; Hayama et al., 2013). Back-propagating action potentials provide a straightforward way to evoke dendritic Ca^{2+} transients that depend on the activation of local voltage-gated Ca^{2+} channels (Christie et al., 1995; Pérez-Garci et al., 2013) and are a prerequisite for spike-timing-dependent plasticity. Indeed, one-photon GABA uncaging has recently been shown to modulate spike-timing-dependent plasticity in spines (Hayama et al., 2013). In addition, locally coordinated remodeling of GABAergic synapses (Bourne and Harris, 2011), which can be driven by experience (Chen et al., 2012), provides indirect evidence that individual GABAergic contacts may orchestrate plasticity. However, the inhibitory impact of individual dendritic GABAergic synapses has not yet been measured under physiological conditions. Studies employing GABA iontophoresis or one-photon GABA uncaging do not reach synaptic resolution: due to the high abundance of extrasynaptic GABA receptors, these methods will not only co-activate nearby inhibitory synapses but also stimulate extrasynaptic receptors. In consequence, a direct demonstration of the interference of individual GABAergic synaptic inputs with dendritic Ca^{2+} processes has been missing so far. Here, we now use paired patch-clamp recordings and Ca^{2+} imaging to show that individual inhibitory synaptic inputs significantly reduce Ca^{2+} transients in dendritic shafts and spines and that this inhibitory action is spatially and temporally precise.

RESULTS

Individual GABAergic Synaptic Contacts Inhibit Dendritic Ca^{2+} Transients

In order to quantify the impact of individual GABAergic dendritic shaft synapses on local Ca^{2+} transients, we performed

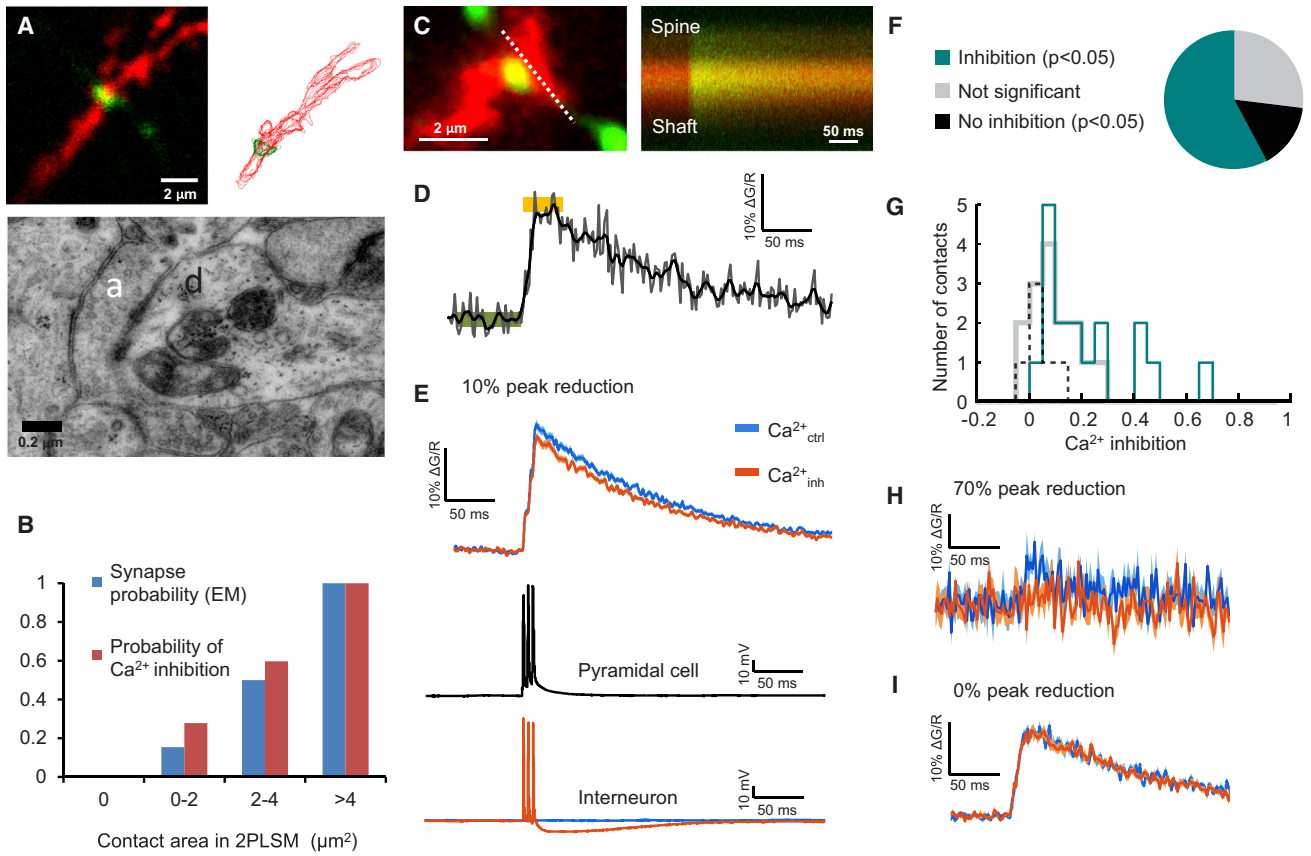

Figure 2. Ca^{2+} Imaging of Synaptic Inhibition

(A) Inhibitory synapse detected in 2PLSM (top left), post hoc verified in EM (bottom), and reconstructed (right). a, axon (green); d, dendrite (red).

(B) Comparison of the probability of finding an inhibitory synapse at a putative contact detected in 2PLSM (blue) and the probability of detecting significant Ca^{2+} inhibition at a contact (red), given its 2PLSM contact area.

(C) Left: 2PLSM image of a dendritic shaft and spine close to a putative inhibitory synapse (yellow); dotted line indicates line scan. Right: AP-evoked Ca^{2+} signal in the dendritic shaft and spine.

(D and E) Ca^{2+} transients in the shaft shown in (C). (D) Single raw (gray) and Gaussian-filtered transient (50 Hz low-pass, black). Green bar, baseline; yellow bar, peak detection region. (E) Top: average unfiltered transients (mean ± SEM), evoked by APs only (blue) or by simultaneous IPSPs + APs (orange). Bottom: corresponding spikes in the pyramidal cell (black) and interneuron (orange, AP; blue, no AP).

(F and G) Proportion of contacts with area > 1 μm^2 (F, n = 26) and distribution of Ca^{2+} inhibition at all contacts (G, n = 38) for which significant inhibition, significant absence of inhibition (<5% reduction), or no significance was reported.

(H and I) Ca^{2+} transients representative for strong inhibition (70%, H) and no inhibition (0%, I); mean ± SEM.

paired patch-clamp recordings from GABAergic interneurons and nearby pyramidal cells in organotypic hippocampal slice cultures prepared from GAD65-GFP mice (López-Bendito et al., 2004). Here we took advantage of the strong GFP expression in a subset of mostly dendrite-targeting GABAergic interneurons (Wierenga et al., 2010). A GFP-positive interneuron with its soma in stratum radiatum/oriens or at the border to stratum pyramidale and a nearby pyramidal cell were patched simultaneously (Figure 1A). We visually confirmed that the interneuron axon contacted the pyramidal cell dendrites (Figure 1B). We additionally checked whether the axon also contacted the soma and found that ~80% of the interneurons did not make contacts with the cell body; in the remaining ~20%, one axon branch contacted the soma with 1–3 boutons but never in a basket-like fashion. Action potentials (APs) in both cells were elicited by somatic current injection. Whenever interneuron stimulation elicited a unitary inhibitory postsynaptic current (IPSC) in the voltage-clamped pyramidal cell, it was taken as evidence for a direct synaptic connection (Figure 1C connection probability ~60%, IPSC amplitude 5–400 pA at −40 mV, latency 1.6 ± 0.6 ms; mean ± SD). Unitary IPSC kinetics were (without exception) intermediately fast (range of half-widths 3.5–13.1 ms at −40 mV, 34°C, see Figure 1C and Table S1), with negative correlations between amplitude and kinetics (Spearman rank correlations with $p < 0.05$), confirming that IPSCs were of dendritic origin and, e.g., neurogliaform cells were not targeted. Morphological and electrophysiological analysis revealed that the selected interneurons were multipolar and displayed regular firing patterns with moderate frequency and/or amplitude

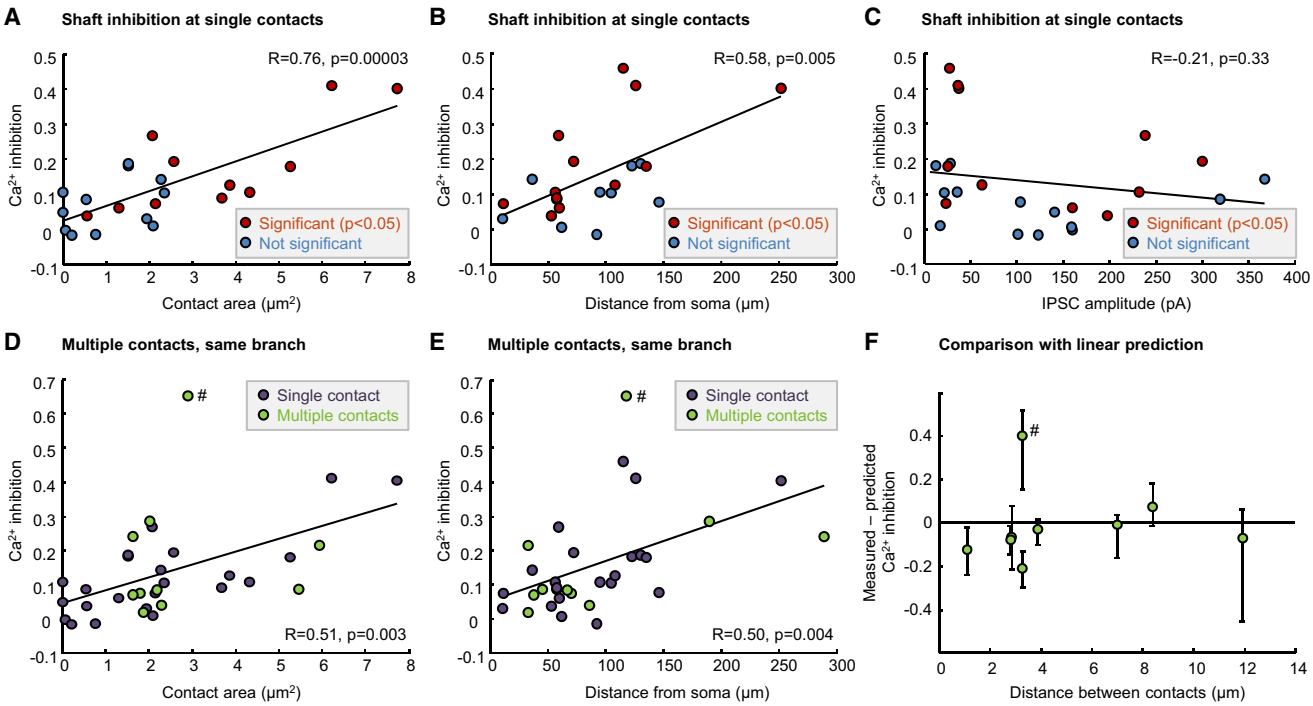

Figure 3. Ca^{2+} Inhibition Depends on Contact Area and Distance from Soma

(A–C) Ca^{2+} inhibition at dendritic shafts carrying single contacts plotted versus axo-dendritic contact area (A), versus distance between contact and soma (B), and versus somatic IPSC amplitude (C). Contacts with significant inhibition are labeled in red, all others in blue. Pearson R include all data; n = 22–24 contacts between n = 18 pairs.

(D and E) Ca^{2+} inhibition recorded at branches carrying multiple contacts (green) is compared to the single contact data (purple) from (A) and (B); n = 32–33 contacts between n = 25 pairs.

(F) Ca^{2+} inhibition measured at multiple contacts is compared to the Ca^{2+} inhibition predicted by their summed contact area, based on an additive linear model of contact area and distance derived from the single contact data. # marks the same data point in (D–F). In (D), contact area of multiple nearby contacts refers to the largest contact area. The contact area of spherical surfaces is $6/\pi \approx 2$-fold overestimated due to the cubic approximation (reported values are uncorrected). Error bars indicate bootstrapped 95% confidence intervals.

adaptation. The firing profiles are consistent with previous reports for VIP- or Reelin-positive CGE-derived interneurons (Miyoshi et al., 2010; Wierenga et al., 2010) and consist of ~50% delayed and (moderately) fast-spiking (20/21 dNSF3), ~20% delayed and regular-spiking (9/10 LS1/2), and ~30% non-delayed, mostly regular-spiking interneurons (5/15 bNA2) (Figures 1D and 1E). Reversal potentials were well within the physiological range, as confirmed by gramicidin perforated-patch recordings (Figure 1F, −69.6 ± 1.5 mV versus 71.4 ± 1.2 mV at 24°C and −74.1 ± 2.2 mV versus −75.3 ± 2.1 mV at 34°C in whole-cell versus perforated, mean ± SEM, differences not significant, n = 9/11/7/5), and stable during whole-cell recordings of the cells (Figures 1G and S1). In summary, the inhibitory interneurons studied were multipolar, regular firing, most likely Reelin or VIP-positive cells.

Structure-Function Correlation

To identify putative inhibitory synaptic contacts, we exhaustively screened a major part of the dendritic tree (~600 µm along the somatodendritic axis) by two-photon laser-scanning microscopy (2PLSM) for morphological contacts between the inhibitory axon and the pyramidal cell dendrite (Figure 1B; 10 ± 5 putative contacts mapped, mean ± SD). EM analysis showed that this procedure readily detects inhibitory synapses (Figure 2A) and that the probability of finding an inhibitory synapse at an identified contact depends on its 2PLSM axo-dendritic contact area (n = 6/26, Figure 2B). Once a putative axo-dendritic contact was identified, Ca^{2+} transients were evoked in the pyramidal cell dendrite by back-propagating APs and measured locally by 2PLSM line scans (Figure 2C). We observed that the amplitude of Ca^{2+} transients could drop substantially when we simultaneously stimulated the interneuron. To quantify this inhibition, we compared Ca^{2+} transients evoked by simultaneous APs and IPSPs (ΔCa^{2+}_{inh}) with AP-evoked Ca^{2+} transients under control conditions (ΔCa^{2+}_{ctrl}, Figures 2D and 2E). We report Ca^{2+} inhibition as $inh = 1 - \Delta Ca^{2+}_{inh}/\Delta Ca^{2+}_{ctrl}$. Since single APs sometimes failed to evoke detectable Ca^{2+} transients in more distal dendrites, and in order to generally improve the signal-to-noise ratio (SNR), we stimulated both cells with short bursts of three APs (5 ms interstimulus interval). Significant Ca^{2+} inhibition ($p < 0.05$ sign-test) occurred in 58% of morphologically identified contacts with a contact area >1 µm^2 (n = 15 of 26, Figure 2F). For a given contact area, the probability of detecting significant Ca^{2+} inhibition was similar to the probability of finding a GABAergic synapse in EM (Figure 2B), indicating that we indeed measured synaptic inhibition. For each contact, the Ca^{2+}

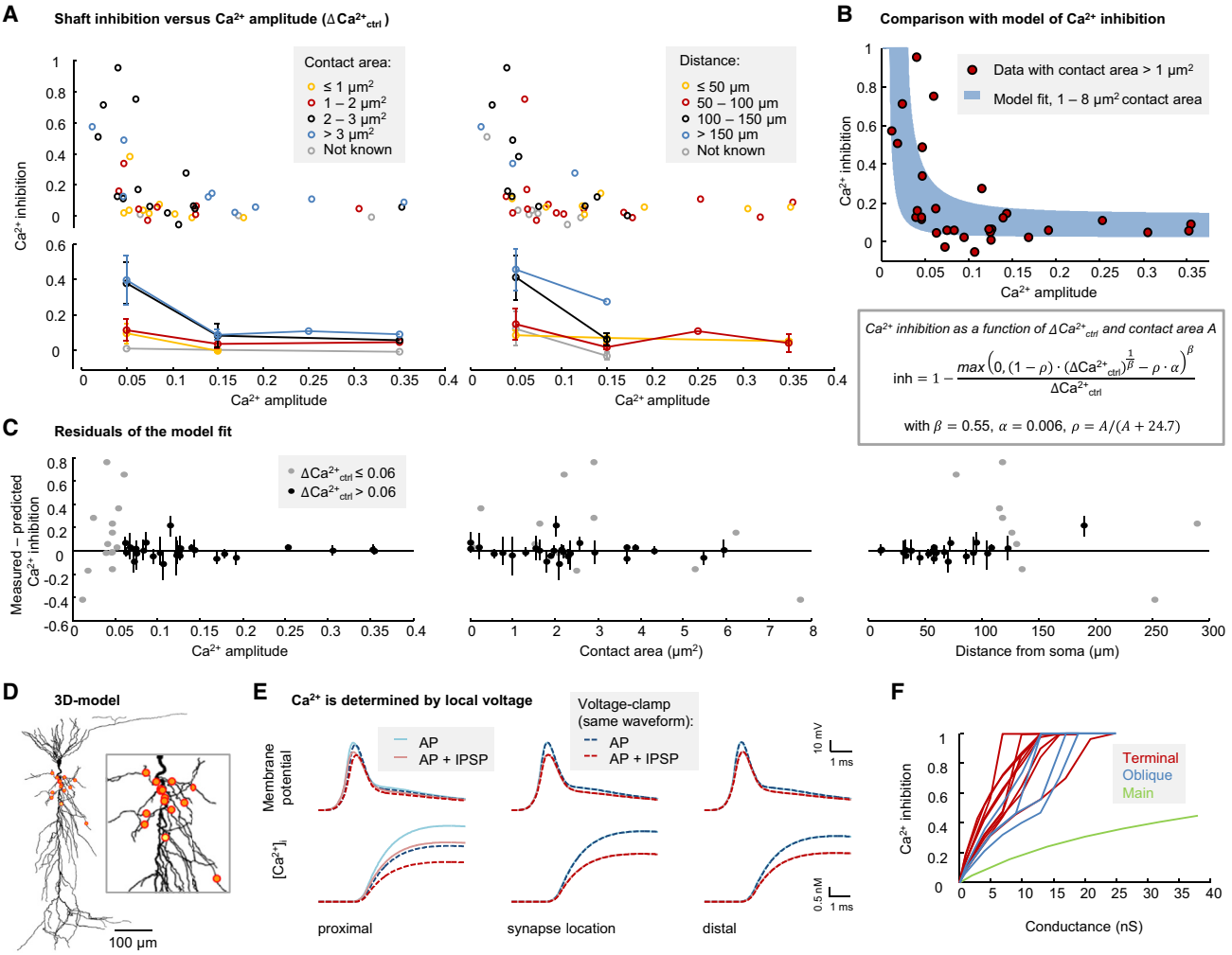

Figure 4. Models of Ca^{2+} Inhibition

(A) Ca^{2+} inhibition at shafts strongly depended on the Ca^{2+} amplitude (ΔCa^{2+}_{ctrl}) for different contact areas (left) and distances (right). Bottom panels present mean ± SEM of data in the top panel, averaged in bins of 0.1 ΔCa^{2+}_{ctrl}.

(B) Top: Ca^{2+} inhibition was well fitted by a function of Ca^{2+} amplitude and contact area, indicating inhibition of VGCCs as the underlying mechanism. Red circles: data from contacts with area 1–8 μm^2; blue area: model fit, plotted for contact areas 1–8 μm^2. The fit was weighted by the inverse of bootstrapped variances. Bottom: model function and fitted parameters. ρ: shunt level, related to contact area *A* as a correlate of inhibitory conductance by $\rho = A/(A+\gamma)$. α, β, γ: free model parameters.

(C) Residuals after fitting the model, plotted versus Ca^{2+} amplitude (left), contact area (middle), and distance from soma (right). Data points with $\Delta Ca^{2+}_{ctrl} \leq 0.06$ are shaded gray, since, due to the reciprocal function, small errors in ΔCa^{2+}_{ctrl} will result in large prediction errors for these data points. Error bars indicate bootstrapped 95% confidence intervals. To avoid overestimation of small transients in (A–C), we quantified ΔCa^{2+}_{ctrl} by averaging ΔG/R over 100 ms, corresponding to ~75% of peak ΔCa^{2+}_{ctrl}.

(D) Shape plot of the multi-compartmental CA1 pyramidal cell model (n123 from Southampton archive). Red circles indicate locations of the 15 randomly distributed synapses (activated one at a time). Inset: zoom-in.

(E) Comparison of recorded membrane potentials (top) and Ca^{2+} transients (bottom) when an AP (blue) or AP + IPSP (red) were elicited (full lines) or when the recorded membrane potential was played back to a voltage clamp at the synapse location (dashed lines). Representative example shown with 4 nS inhibitory conductance (synapse location yellow in D).

(F) Relationship between maximum Ca^{2+} inhibition and inhibitory conductance at the 15 randomly distributed synapses. Colors code for branch type (terminal oblique/oblique/main apical).

inhibition under optimal conditions (optimal spike-timing and distance from contact) was quantified. Ca^{2+} inhibition varied largely and reached values up to 70% (representative traces for different inhibition levels shown in Figures 2E, 2H, and 2I). With a median inhibition of 8.8% across all contacts (n = 38, Figure 2G), and 17.9% across contacts where inhibition reached significance (n = 17), Ca^{2+} transients were only modulated in amplitude, but not completely blocked.

Ca^{2+} Inhibition Is Determined by Local Factors

To characterize dendritic Ca^{2+} inhibition in more detail, we first asked what the main determinants of Ca^{2+} inhibition are. While

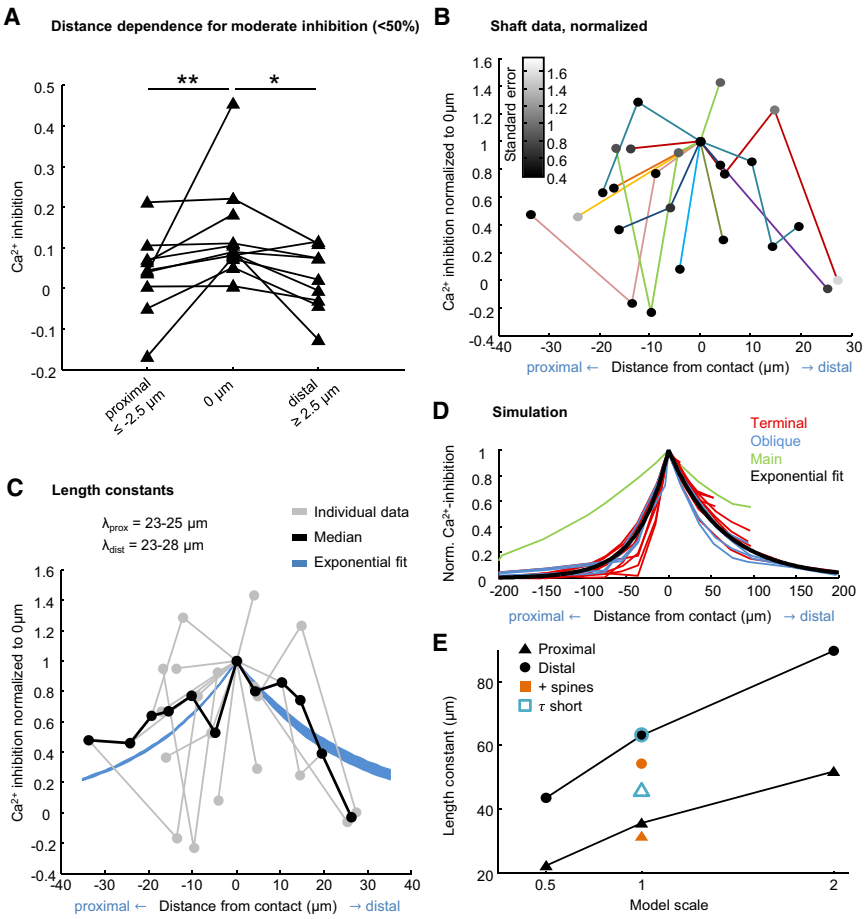

Figure 5. Ca^{2+} Inhibition Is Distance Dependent

(A) Comparison between average inhibition at the contact (0 µm) and ≤−2.5 µm or ≥2.5 µm away from the contact revealed that inhibition significantly drops in both directions (n = 10, p = 0.002 proximal, n = 9, p = 0.04 distal, sign test; one data series with Ca^{2+} inhibition < 0 at 0 µm was excluded which did not affect significance).

(B) Shaft Ca^{2+} inhibition for varying distances between imaging line and inhibitory contact, normalized to the Ca^{2+} inhibition at 0 µm for each dataset. Grayscale indicates the error estimated by bootstrapping and error propagation. Data with Ca^{2+} inhibition > 0.5 was separately analyzed (Figure S3B). Colors code different contacts.

(C) Normalized shaft data (gray) and median per 5 µm (black). Blue areas indicate the range of length constants estimated with sliding threshold over the full dataset (n = 3–14 contacts in n = 12 cells). Data points with error ≥ 1.75 were omitted in (B) and (C) but were included in the variance-weighted fit. The one data series with <0 Ca^{2+} inhibition at 0 µm was excluded before normalization.

(D) Simulated spatial profile of Ca^{2+} inhibition (maximum < 30%) at optimal spike-timing, normalized to its maximum. Black line: exponential fit. Colors code for branch type.

(E) Length constants vary with model parameters. Black, length constants of the simulated Ca^{2+} inhibition profile after scaling the model in size by 2 or 0.5. Orange: spines added with density 0.5/µm along the recorded branches. Blue: α-synapse with τ = 0.5 ms instead of 1 ms. Circles: distal; triangles: proximal length constants.

local Ca^{2+} inhibition was highly correlated with axo-dendritic contact area (Pearson R = 0.76, p < 0.001, Figure 3A), it was only moderately correlated with the distance from the soma (Pearson R = 0.58, p = 0.005, Figure 3B) and completely uncorrelated with the somatically measured compound IPSC amplitude (Pearson R = −0.21, p = 0.33, Figure 3C), arguing against the possibility that the observed dendritic inhibition was due to a global interference of the compound IPSP with the AP or its back propagation. Measurements from dendritic spines cross-validated our results: Ca^{2+} inhibition at dendritic spines also depended on contact area (Figure S2A) but not IPSC amplitude (Figure S2B).

Ca^{2+} Inhibition at Multiple Contacts

The data shown so far were acquired at dendrite sections carrying single inhibitory contacts. Additionally, in ~30% of dendrite sections, we found multiple contacts nearby on the same branch (2–3 contacts within 1–12 µm) and we wondered whether these contacts could interact. Ca^{2+} inhibition at multiple contacts depended in a similar way on the largest contact area and distance from soma (Figures 3D and 3E), and for most contact pairs, Ca^{2+} inhibition was equal or even smaller than predicted by the summed contact area (based on a linear model fit to single contact data, Figure 3F). This suggests that multiple contacts on the same dendritic branch did not interact but added their effect (sub)linearly.

Ca^{2+} Inhibition Can Be Modeled as a Function of Peak Calcium and Contact Area

One pair of contacts with exceptionally strong inhibition (marked by # in Figures 3D–3F; 5.4 $µm^2$ summed contact area) caught our eye. Since it had an unusually small Ca^{2+} transient, we looked more closely at the relation between Ca^{2+} inhibition and Ca^{2+} transient amplitudes. For contacts on distal dendrites at which ΔCa^{2+}_{ctrl} was close to baseline fluctuations, we additionally applied bursts of 4 APs to the pyramidal cell (n = 3) to increase Ca^{2+} amplitudes. When we compared Ca^{2+} inhibition from both stimulation paradigms to the respective Ca^{2+} amplitude without inhibition, we found a striking, yet nonlinear correlation (Figures 4A and 4B, Spearman R = −0.59, p = 0.0006 for contacts > 1 $µm^2$), indicating that inhibition was significantly larger for small Ca^{2+} transients. This finding was consistent across different contact areas and distances (Figure 4A left and right) and also observed in spines (Figure S2C). We next derived a basic model describing inhibition of a thresholded voltage-dependent mechanism as a function of Ca^{2+} amplitude and inhibitory conductance (see Supplemental Information), which provided an excellent fit to the data

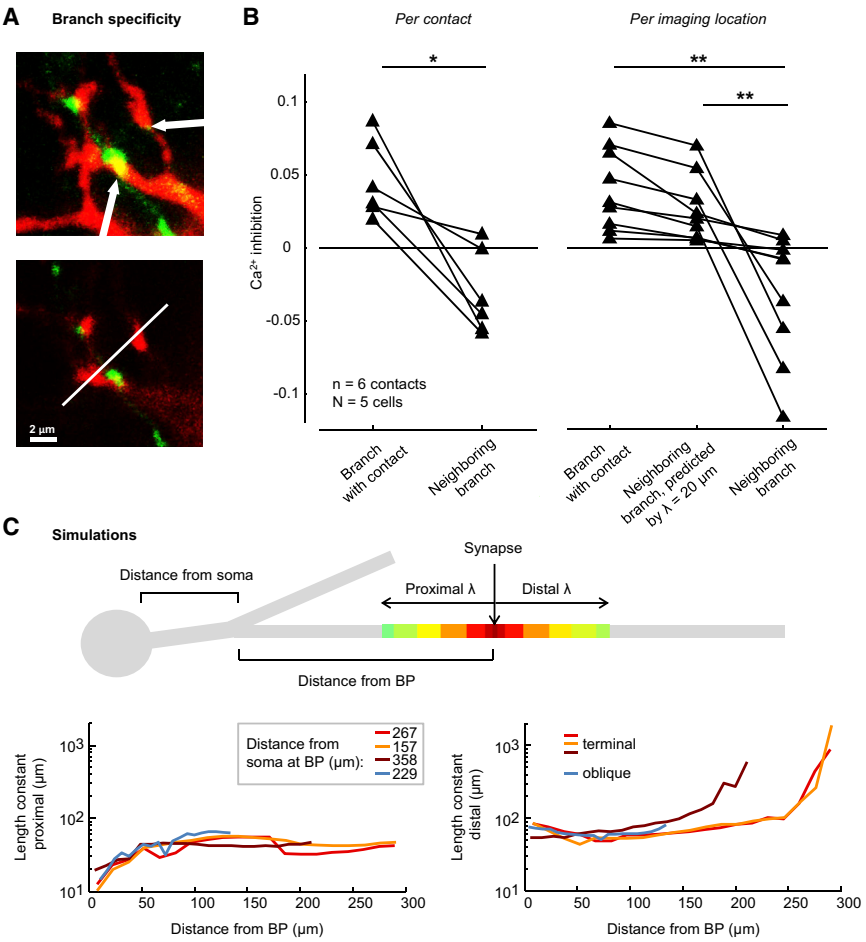

Figure 6. Ca^{2+} Inhibition Is Branch Specific

To measure differences in Ca^{2+} inhibition between branches, we analyzed paired data from simultaneous recordings at two neighboring branches.

(A) Example configuration for a paired dataset; top: maximum projection, arrows point at branch with inhibitory contact and its neighboring branch; bottom: single z plane, line scan over both branches indicated by white line.

(B) Left: pairwise comparison between Ca^{2+} inhibition at branches with inhibitory contact and their neighboring branches (n = 6 contacts, p = 0.03 sign test, average across different imaging locations). Right: for every imaging location, Ca^{2} inhibition at the neighboring branch was corrected for the distance along the dendritic axis, based on a length constant of 20 µm. Ca^{2+} inhibition at the neighboring branch was significantly smaller than the distance-corrected values (p = 0.004 sign test, n = 9 imaging locations).

(C) Simulated proximal (bottom left) and distal (bottom right) length constants for synapses with varying distance from a branch point (BP). Simulations are shown for optimal spike-timing. Colors code different branches. Top: simulation scheme.

(Figure 4B). As the model predicts, transients of small (slightly super-threshold) amplitude can be blocked by a comparably small inhibitory shunt. Analysis of the residuals shows that the model fully accounts for the observed relation between Ca^{2+} inhibition, Ca^{2+} amplitude, and contact area as a correlate of conductance (Figure 4C). Also, most of the increase of Ca^{2+} inhibition with distance from the soma is accounted for by the model, suggesting that part of the correlation seen in Figure 3B is a secondary effect of decreased Ca^{2+} amplitude with distance (Figure 4A, right). Therefore, the reduction in membrane potential that, in turn, reduces activation of voltage-gated Ca^{2+} channels (VGCCs) can mechanistically explain the strong dependence of Ca^{2+} inhibition on Ca^{2+} amplitude.

A Model for the Spatiotemporal Profile of Ca^{2+} Inhibition

While our simplified model of Ca^{2+} inhibition fits the data very well, it ignores the spatial and temporal dynamics of both the back-propagating AP and the IPSP. To account for these and help us interpret the following experiments mechanistically, we set up a multi-compartmental CA1 pyramidal cell model with detailed morphology, voltage-gated channel distributions, and calcium dynamics (Figure 4D, based on Poirazi et al., 2003, for modifications see Supplemental Experimental Procedures). Inhibitory synapses were randomly placed across the proximal third of the apical dendritic tree, across which Ca^{2+} responses were evoked by back-propagating APs. In the 3D model, we could simultaneously record Ca^{2+} transients and membrane potentials associated with back-propagating APs, with and without activation of an individual inhibitory synapse. When we clamped the dendrite to the recorded voltage waveforms, the same Ca^{2+} transients were induced at the synapse location and downstream in the dendrite, indicating that the local dendritic membrane potential fully dictates Ca^{2+} influx through VGCCs (Figure 4E). The level of Ca^{2+} inhibition increased roughly linearly (on average slightly sublinearly) with inhibitory conductance (Figure 4F) in accordance with our data (Figures 3A and 3D). These results are in agreement with the simple model and show that Ca^{2+} inhibition can be explained by a local reduction of dendritic membrane potential.

Ca^{2+} Inhibition Is Highly Spatially Confined

Our finding that Ca^{2+} inhibition is highly correlated with the local Ca^{2+} amplitude and contact area, but not with the global IPSC amplitude, strongly indicated that individual inhibitory contacts have a localized impact. We therefore wanted to determine the spatial (and temporal) precision of inhibition exerted by individual GABAergic synapses. To experimentally map the spatial profile of Ca^{2+} inhibition along the dendrite, we systematically varied the distance between the imaging line and the synaptic contact. We found that inhibition of Ca^{2+} transients was significantly reduced >2.5 µm proximally and distally of the contact (Figure 5A, $p < 0.05$, sign-test). After normalizing Ca^{2+} inhibition to the value measured at 0 µm (Figure 5B), length constants of

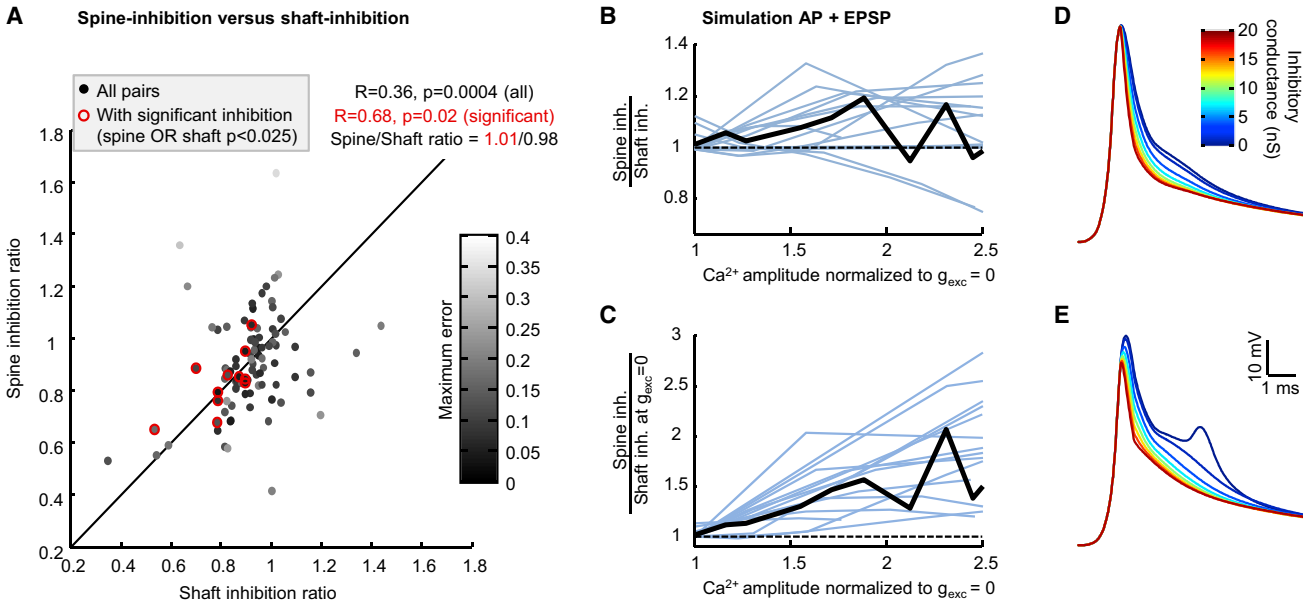

Figure 7. Ca^{2+} Transients Are Equally Inhibited in Spines and Shafts

(A) Pairwise comparison of Ca^{2+} inhibition in individual dendritic spines and their neighboring shafts, averaged per stimulation protocol (94 protocols for n = 65 spines in n = 23 cells). We used here Ca^{2+} inhibition ratios ($1 - inh$) to avoid division by negative numbers when estimating the median ratio between spine inhibition and shaft inhibition ("Spine/Shaft ratio"). Pearson correlation coefficients are indicated. Solid line is the unity line.

(B–E) Simulated pairing of a back-propagating AP and an EPSP arriving at a spine next to the inhibitory shaft-synapse; EPSP 2 ms delayed (LTD protocol). (B) Maximum Ca^{2+} inhibition at the spine head relative to the shaft, for varying excitatory conductances (relative increase of Ca^{2+} amplitude on the x axis). Average across spines in black. (C) Same as (B) but normalized to the shaft Ca^{2+} inhibition for the AP alone. (D and E) Example membrane potentials recorded at the spine head for varying inhibitory conductances (color code).

22.6–24.9 μm proximal and 22.9–27.5 μm distal were estimated by variance-weighted exponential fitting (Figure 5C). Ca^{2+} inhibition in spines exhibited a similar bidirectional decline (Figure S3A). Exceptionally strong inhibition, on the other hand, could propagate further into the distal compartment (Figure S3B). The results were in line with our model simulations (Figure 5D), which also showed an exponential and bidirectional decline of Ca^{2+} inhibition for moderate inhibition levels. To understand quantitative differences between the simulation and data, we explored some key parameters. Consistent with the shorter length constants and the smaller cell size in our data (mice organotypic slice culture, compared to rat acute slice), length constants scaled with the model size (Figure 5E). Length constants were additionally shortened by ~13% if spines were added along the recorded branches with density 0.5/μm (orange symbols). A more symmetric profile (better matching our data) was achieved, e.g., by slightly more delayed inhibition (see full spatiotemporal profile further below) or faster synapse kinetics (blue symbols).

Ca^{2+} Inhibition Is Branch Specific

In addition to its high spatial precision, Ca^{2+} inhibition was also branch specific: when we simultaneously recorded from a dendritic branch that carried an inhibitory contact and from one of its neighboring branches, inhibition dropped significantly between them (Figures 6A and 6B). Importantly, inhibition dropped significantly more between branches than predicted based on the average length constants and the respective distances along the dendritic axis (right panel). According to the model, one major biophysical mechanism that promotes branch specificity of Ca^{2+} inhibition is that branch points act as a current sink and proximal length constants get smaller toward the branch points (Figure 6C, left), which is the opposite of the sealed-end effect which produces an increase of distal length constants toward branch terminals (Figure 6C, right).

Ca^{2+} Amplitudes in Spines and Shafts Are Inhibited to the Same Degree

Having observed the pronounced spatial confinement of Ca^{2+} inhibition along the longitudinal dendritic axis, we wondered whether Ca^{2+} inhibition would also be attenuated transversely between dendritic shafts and spines. Since theoretical studies have predicted that, due to chloride accumulation, $GABA_A$-receptor-mediated inhibition will be ineffective on spines (Qian and Sejnowski, 1990), we focused on inhibitory shaft synapses, which are overall more abundant (Megías et al., 2001). Hence, the majority of inhibitory contacts in our dataset were located on dendritic shafts (87%, n = 48/55), while only 9% (5/55) were located on spine heads, and another 4% (2/55) contacted shaft and spine. Notably, at each contact the average Ca^{2+} inhibition under optimal conditions was highly correlated between spines and shafts (Pearson $R = 0.73$, $p < 0.0001$). However, since spines had an average minimum distance of 1.6 μm to the

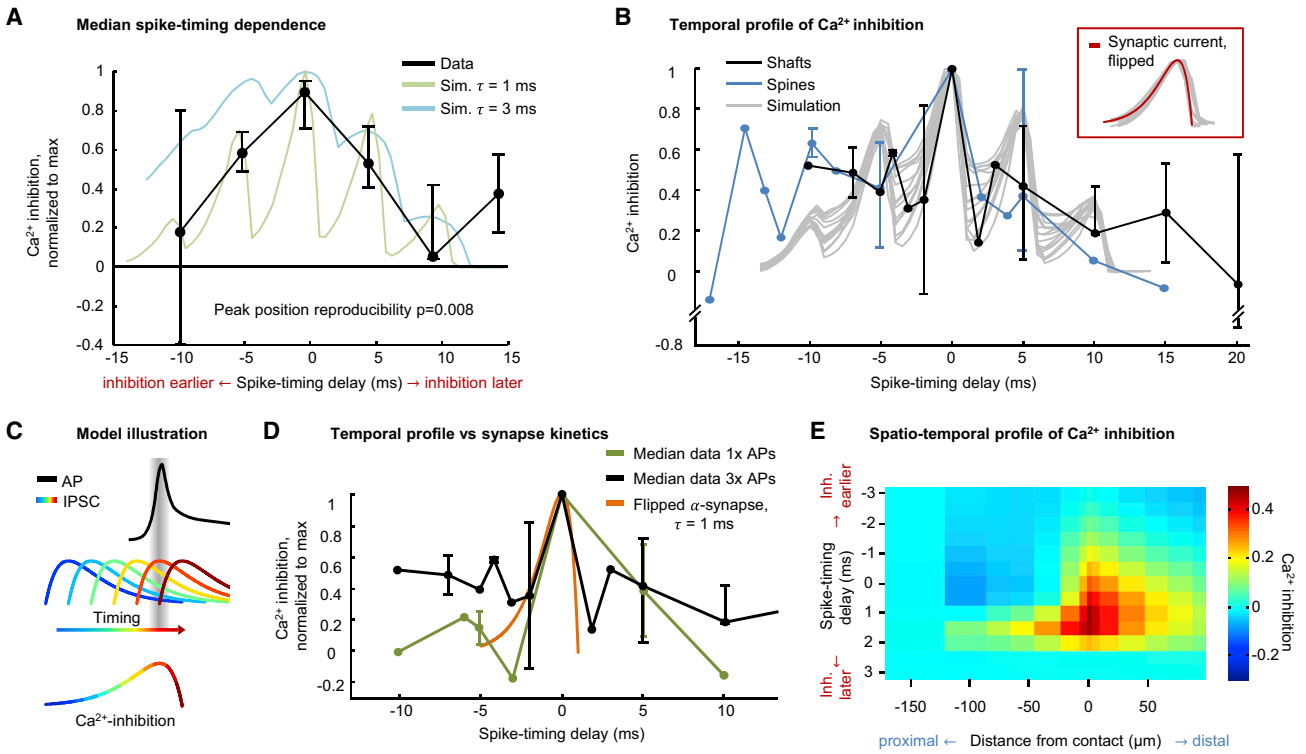

Figure 8. Ca^{2+} Inhibition Is Spike-Timing Dependent

(A) Median Ca^{2+} inhibition measured by 3× stimulation in dendritic shafts, plotted versus spike-timing delay. Ca^{2+} inhibition for each dataset was normalized to its maximum, before calculating the median per 5 ms bin. The optimal spike-timing was reproducible within most datasets (p = 0.008 in shafts, n = 10, p = 0.04 in spines, n = 9). Light blue/green lines are representative examples for simulated Ca^{2+} inhibition profiles of 3× APs, shifted to optimal spike-timing. 3× α-synapse simulated with τ = 3 ms (blue) or τ = 1 ms (green). Note the higher-frequency modulation for fast kinetics.

(B) When the data were aligned to respective optimal spike-timing and binned with 1 ms bins, a similar periodicity was observed in shafts (black) and spines (blue) as in the simulation for τ = 1 ms (gray). Inset: the simulated spike-timing dependence of Ca^{2+} inhibition (1× stimulation in gray) is a mirror image of the synapse kinetics (flipped synaptic current in red).

(C) Model illustration of a time-variant IPSC (colors indicate successive time points) interacting with a time-invariant AP, resulting in a flipped time course of inhibition. For negative spike timing, the decaying flank of the IPSC coincides with the AP, while for positive spike-timing, the rising flank coincides with the AP.

(D) Aligned 3× stimulation data (black) and 1× stimulation data (green) from shafts provide an upper estimate of synapse kinetics and are well fit by an α-synapse with τ = 1 ms (orange). (A–D) Medians and bootstrapped 68% confidence intervals shown, no error bars for singular observations. Medians included only data with significant Ca^{2+} inhibition > 0.085 (3× AP data) or Ca^{2+} inhibition > 0.085 (1× AP data in D). For aligned data (B and D), only data with cross-validated optimal spike-timing are shown to avoid noise fitting: 8/11 (shafts) and 5/9 (spines) in (B), 4/8 (1× AP) in (D). Cross-validation was significantly above chance level over a broad range of threshold choices (0–0.23 for shafts).

(E) Representative example for the spatio-temporal profile of Ca^{2+} inhibition around an individual inhibitory synapse. Taking synaptic and AP onset delays into account, the simulation is about +1.3 ms shifted compared to the data.

inhibitory contact, an exact quantification of attenuation required the pairwise comparison between equidistant spines and shafts. Remarkably, when we analyzed paired data acquired at spines and their neighboring shafts, Ca^{2+} inhibition was equally strong in both spine and shaft (Figure 7A, Pearson R = 0.36, p = 0.0004, median ratio $[1 - inh_{spine}]/[1 - inh_{shaft}] = 0.98$ per individual spine/shaft pair). To rule out that a potential attenuation could be obscured by data points exhibiting little inhibition or low SNR, we selected the subset of data showing significant inhibition (sign-test with p < 0.025 in the spine or shaft). This unbiased criterion was met in nine spines, all with neck length <1 µm, and all in proximity (1–4 µm) to a shaft contact or a combined shaft+spine contact. Like in the full dataset, we observed no detectable attenuation along the spine neck (Pearson R = 0.68, p = 0.02, median ratio $[1 - inh_{spine}]/[1 - inh_{shaft}] = 1.01$). In conclusion, the inhibition of Ca^{2+} transients spreading from the shaft to the spine is not attenuated along the spine neck.

In our model, this result was fully reproduced with spines of the average geometry suggested by the latest STED measurements (Tønnesen et al., 2014). Moreover, when we added an excitatory synapse on the spine, which was activated with delay to the AP (mimicking an LTD protocol), inhibition of the combined Ca^{2+} response could be even stronger in the spine than in the shaft for moderate excitatory conductances (Figure 7B, data shown with maximum 30% shaft inhibition). And even more importantly, Ca^{2+} inhibition increased with the EPSP size (Figure 7C), since inhibition mechanistically acts by reducing the afterdepolarization around threshold for VGCCs (Figure 7D) or even blocking secondary spikelets (Figure 7E), which is both comparable to the supralinear inhibition of small Ca^{2+} signals that we have

observed (Figures 4A–4C). Our results suggest that Ca^{2+} inhibition by shaft synapses is on average equally effective in the spine and in the shaft and that inhibition of Ca^{2+} signals in the presence of synaptic input can be much stronger than inhibition of APs alone.

Ca^{2+} Inhibition Is Spike-Timing Dependent

Synaptic integration and plasticity often depend crucially on the exact timing of different inputs, as exemplified by phenomena like spike-timing-dependent plasticity (Bi and Poo, 1998). In order to test the temporal precision of Ca^{2+} inhibition, we systematically varied the timing between pre- and postsynaptic APs and found that Ca^{2+} inhibition was strongly spike-timing dependent. On average, maximum inhibition occurred for simultaneous spikes (0 ms delay) and declined to its half-maximum within ±5–10 ms (Figure 8A). While the timing at which maximum inhibition occurred ("optimal spike-timing") exhibited some variation between inhibitory contacts, it was reproducible within most datasets (7 out of 10, corresponding to $p = 0.008$). Comparing the data with simulations based on different synapse kinetics (Figure 8A, $\tau = 1$ or 3 ms) suggested that the observed spike-timing dependence reflects fast synaptic currents. With fast synapse kinetics, the model further predicts a modulation of Ca^{2+} inhibition at smaller timescales and, indeed, after aligning the cross-validated data to their optimal spike-timing, the median data showed a similar periodicity (Figure 8B). Furthermore, the model showed that the spike-timing profile of Ca^{2+} inhibition has the interesting property of being a mirror image of the synaptic current (Figure 8B, inset), which indicates that the underlying mechanism of Ca^{2+} inhibition is a direct interaction between the inhibitory current and a fast AP-mediated process (Figure 8C), like VGCC activation as suggested by our simplified model. Consistent with the simulation, the spike-timing profile around 0 for triple stimulations matched a (lower SNR) dataset acquired using single APs (Figure 8D). Both were reasonably well fit by an α-synapse current with time constant 1 ms (a simple synaptic conductance model, orange trace in Figure 8D), providing a (noise-limited) estimate for the kinetics of an individual GABAergic synaptic contact. Expectedly, the estimated kinetics of individual GABAergic synaptic inputs on dendrites is considerably faster than IPSC kinetics measured at the soma (Table S1) due to dendritic filtering. Notably, the simulated spike-timing profile was unchanged when we scaled the model to different sizes (data not shown), suggesting that our main conclusions in all likelihood will also hold (in a scaled fashion) in different model systems/animals.

Finally, we used the model to predict the two-dimensional spatio-temporal profile of Ca^{2+} inhibition (Figure 8E). Besides demonstrating the high spatio-temporal precision of Ca^{2+} inhibition, the 2D profile gives two more insights. First, the two variables space and time are not independent, but the temporal profile becomes more symmetric for more delayed inhibition. Second, at earlier timing Ca^{2+} inhibition can be inverted (darker blue areas in Figure 8E) and effectively increase Ca^{2+} amplitudes by a small amount, which corresponds to a subtle broadening of the AP, e.g. due to a hyperpolarization-mediated relief of calcium and/or sodium channels from inactivation. This may explain the observed trend toward inverted Ca^{2+} inhibition at neighboring branches (right panel in Figure 6B, not significant) and suggests that this is not a branch-specific effect per se.

DISCUSSION

Taken together, our data show that individual GABAergic synapses on dendritic shafts significantly inhibit Ca^{2+} transients from back-propagating APs within a narrow spatial and temporal window (length constant 23–28 μm, time constant < 5 ms) and that Ca^{2+} transients in dendritic spines are inhibited to the same degree as in shafts. While the degree of Ca^{2+} inhibition is overall moderate (Figure 2G, median inhibition 17.9% where significance was reached), it is nevertheless in a range that is likely to be physiologically relevant.

Ca^{2+} Inhibition and Synaptic Plasticity

For instance, long-term potentiation depends steeply on the dendritic Ca^{2+} amplitude and is therefore sensitive even to small changes (Nevian and Sakmann, 2006, see their Figure 8). In a GABA-dependent long-term depression paradigm, a robust induction of spine shrinkage corresponded to only 20%–30% average reduction in Ca^{2+} amplitude (Hayama et al., 2013). Although our data are limited to the inhibition of back-propagating action potentials, our model predicts that in an LTD protocol, Ca^{2+} inhibition of the combined EPSP+AP can be even larger than Ca^{2+} inhibition of the AP alone, suggesting that individual GABAergic synapses will be able to promote LTD at nearby spines. Moreover, our model provides a mechanistic explanation for the results of Hayama et al. (2013): inhibition can drive the membrane potential below the VGCC threshold or block secondary local spikelets induced by the EPSP, comparable to the supralinear inhibition of small bAPs (Figures 4A and 4B). While the low abundance of dendritic spines receiving inhibitory synapses (<10%; Megías et al., 2001) might have suggested that only a subset of excitatory synapses can be directly modulated by inhibition, our data indicate that potentially all spines can be controlled by shaft inhibition in the vicinity. Thus our data indicate that individual inhibitory shaft synapses have the potential to orchestrate synaptic plasticity and other Ca^{2+}-dependent processes at the surrounding dendritic spines.

Ca^{2+} Inhibition Acts via Membrane-Potential Reduction

Our model demonstrates that the underlying biophysical mechanism of Ca^{2+} inhibition is the reduction in the voltage waveform of the back-propagating AP, which dictates the magnitude and time course of Ca^{2+} influx via the VGCCs (Figure 4E). It should be noted, however, that the spatiotemporal profile of voltage inhibition (measured as inhibition of spike amplitude) is not exactly the same as that of Ca^{2+} inhibition. The main reason for this mismatch is that activation of VGCCs depends on the complex waveform, not only on the amplitude of the spike. But also local properties can vary, such that the same AP waveform can result in different Ca^{2+} influx in different compartments. The interaction between IPSPs and APs that we studied here can be viewed in close analogy to the interaction between EPSPs and APs, which has been shown to also depend on the interference with voltage-dependent conductances and underlie a sharp (albeit less sharp) spike-timing dependence (Stuart and Häusser, 2001, temporal profile is in their case similar to the EPSP, not EPSC waveform).

Ca^{2+} Inhibition Has a Large Dynamic Range

The fact that inhibitory contact area is, after Ca^{2+} amplitude, the second major determinant of Ca^{2+} inhibition (Figures 3 and 4), predicts that not only coarse structural remodeling of inhibitory synapses (van Versendaal et al., 2012; Chen et al., 2012), but also gradual changes in synaptic strength can significantly alter levels of dendritic inhibition. Most interestingly, the dependence of Ca^{2+} inhibition on contact area (Figures 3A and 3D) respectively synaptic conductance (Figures 4B and 4F) suggests that changes in inhibitory synaptic strength can dynamically modulate calcium over a broad parameter range.

Considering realistic network activity, it is important to ask how multiple, simultaneously active inhibitory inputs will interact on the dendrite. Our data and model suggest that Ca^{2+} inhibition scales roughly linearly (slightly sublinearly) with conductance (Figures 3A and 4F), so for an average unitary Ca^{2+} inhibition of 15%, it needs ~16 coactive synapses (simulation average, uniformly distributed over ± λ) to fully block the Ca^{2+} transient, corresponding to 0.35 synapses/μm for λ = 23 μm. For larger neurons with presumably longer length constants (Figure 5E), an even lower synapse density would suffice (empirically found density for rat CA1 pyramidal neurons: 0.1–0.6/μm, Megías et al., 2001). In conclusion, different patterns of network activity will cover the full dynamic range of dendritic Ca^{2+} modulation, reaching from the moderate modulation (0%–70%) of Ca^{2+} transient amplitude by unitary connections, which we describe here, to the full blockade of Ca^{2+} spikes by activation of inhibitory microcircuits, which others have observed (Miles et al., 1996; Müller et al., 2012).

Branch Specificity of Ca^{2+} Inhibition

Our observation that dendritic inhibition did not propagate into neighboring branches is in line with other recent data looking at compartmentalization of dendritic inhibition on a broader scale (Marlin and Carter, 2014; Stokes et al., 2014) and supports the view of the dendritic branch as a fundamental processing unit (Branco and Häusser, 2010). In addition to branch-specific mechanisms which strengthen excitability (Losonczy et al., 2008), branch specificity of inhibition might provide an important basis for the inhibition dependence of branch-specific Ca^{2+} spikes (Cichon and Gan, 2015) and for dendritic information storage. Our model indicates that branch specificity is promoted by branch points acting as current sinks. For future studies, it will be interesting to investigate further how additional properties—like branch-point-specific channel distributions—can contribute to this phenomenon.

The Temporal Profile of Ca^{2+} Inhibition Reflects Synaptic Dynamics

Previous studies addressing the spatial or temporal precision of dendritic inhibition have employed one-photon GABA uncaging (Kanemoto et al., 2011; Hayama et al., 2013) or GABA iontophoresis (Liu, 2004; Hao et al., 2009) to activate $GABA_A$ receptors. They led to important insights but—due to the artificial release of GABA—also have important methodological limitations: (1) synaptic specificity cannot be ensured (a limitation which is aggravated by the high abundance of extrasynaptic $GABA_A$ receptors), and (2) local amplitudes, amplitude variations, and kinetics of individual synaptic responses are unknown and can hence not be mimicked. Thus, our data provide the first experimental evidence that synaptically mediated Ca^{2+} inhibition is spike-timing dependent in the millisecond range. Along these lines, it is interesting to note that, consistent with our finding that Ca^{2+} inhibition is most effective for synchronous spike-timing, most dendrite-targeting interneurons fire in synchrony with pyramidal cells at the trough of theta rhythm or at the ascending phase of the theta rhythm when phase-precessing pyramidal cells start firing (Klausberger, 2009).

Surprisingly, our model showed that the spike-timing dependence of Ca^{2+} inhibition is actually a mirror image of the synaptic current. Therefore our data provide (to our knowledge) the first local measurement of inhibitory currents from individual synaptic contacts. While our data do not have the time resolution to fully resolve the synaptic dynamics, the α-synapse fit with time constant of 1 ms (corresponding to 2.4 ms half-width and ~2 ms mono-exponential decay time constant from peak) provides a noise-limited estimate for dendritic $GABA_A$ synapse kinetics, which is in the range of previous indirect estimates for fast GABAergic synapses (Bartos et al., 2001) and emphasizes that somatically measured IPSCs largely overestimate kinetics of remote synapses due to dendritic filtering. In future, our method might also be a valuable approach to measure the time course of IPSCs and its variation between individual contacts, since it allows a local optical readout which is not limited by indicator kinetics.

Ca^{2+} Inhibition in Spines

Since the spine neck limits diffusion between the shaft and the spine head over timescales of 20–100 ms (Svoboda et al., 1996), the Ca^{2+} inhibition that we measure in spines reflects inhibition of VGCCs in the spine head, rather than passively reflecting Ca^{2+} inhibition in the shaft (Sabatini and Svoboda, 2000; we obtained equivalent results to Figure 7B with amplitudes detected within 20 ms, data not shown). The question of how Ca^{2+} signals in spines can be inhibited by GABAergic synapses on either spines or shafts has recently received a lot of attention. Two studies using an approach with larger scale and lower resolution than ours (multicellular optogenetic stimulation plus GABA uncaging) came to opposing conclusions. The first study concluded that Ca^{2+} inhibition resulting from GABAergic spine synapses is highly compartmentalized to spines (Chiu et al., 2013); the second study concluded that dendritic GABAergic synapses inhibit Ca^{2+} transients to the same degree in spines and shafts (Marlin and Carter, 2014). Chiu et al., however, selected spines carrying potential synapses (or "hot spots" of uncaging responses) based on the average Ca^{2+} inhibition and subsequently used the same dataset for comparing average Ca^{2+} inhibition between selected spines and neighboring spines and shafts. This procedure results in a bias toward stronger inhibition in the selected spines, and spine inhibition is therefore overestimated. We now show with synaptic resolution that Ca^{2+} inhibition mediated by shaft synapses shows no detectable attenuation in spines (at least for back-propagating APs). The result was reproduced, also in the presence of EPSPs, in our model, which explicitly considered chloride accumulation (a factor that severely affects inhibition on

spines or very small branches, also see Qian and Sejnowski, 1990).

Limitations of the Study

The scalability of the model (Figure 5E) suggests that our conclusions do not depend on cell size and will also hold (in a scaled fashion) in different model systems/animals. Nevertheless, differences in synaptic conductance or kinetics between the slice culture and in vivo situation would influence the amplitudes (Figure 4F) or temporal profiles (Figure 8D) of Ca^{2+} inhibition. Our study can only provide first estimates here. Furthermore, our model predictions on how exactly inhibition acts on concomitant APs and EPSPs await future experimental investigation.

Conclusion

Relating the spatial spread of Ca^{2+} inhibition that we observed to the density of GABAergic synapses on pyramidal cell dendrites (Megías et al., 2001; Bourne and Harris, 2011), it is clear that GABAergic synapses form a functionally dense network, providing inhibitory control over basically every spot on the dendrite. Together with our observation that Ca^{2+} inhibition reaches comparable levels in spines and in shafts, this suggests that the collective inhibitory input to a pyramidal cell is sufficient to control dendritic Ca^{2+} levels across the whole dendritic arbor with micrometer and millisecond precision.

EXPERIMENTAL PROCEDURES

Organotypic Slice Culture Preparation

All experimental procedures were carried out in compliance with the institutional guidelines of the Max Planck Society and the local government (Regierung von Oberbayern). Hippocampal slices (350 μm thick) were prepared from postnatal day 4–6 GAD65-GFP (Wierenga et al., 2010; López-Bendito et al., 2004) or C57Bl/6 mice and maintained in culture for 2–6 weeks following standard protocols (Stoppini et al., 1991, medium glucose reduced to 5.7 mg/ml).

Electrophysiology

Whole-cell patch-clamp recordings were obtained at 34°C from pyramidal cells (mostly CA1) and interneurons with their somata located in stratum radiatum/oriens or adjacent to stratum pyramidale using a Multiclamp 700B amplifier (Molecular Devices), Bessel filtered at 6 kHz (voltage clamp) or 10 kHz (current clamp), and digitized at 20 kHz (Digidata 1440A). ACSF contained 126 mM NaCl, 2.5 mM KCl, 2.5 mM $CaCl_2$, 1.3 mM $MgCl_2$, 1.25 mM NaH_2PO_4, 26 mM $NaHCO_3$, 20 mM glucose, 0.2 mM Trolox (6-hydroxy-2,5,7,8-tetramethylchroman-2-carboxylic acid). Borosilicate glass capillaries (1.5/0.86 mm od/id, Harvard apparatus, 3–7 MΩ) were filled with internal solution containing 142.5 mM K-gluconate, 7.5 mM KCl, 10 mM HEPES, 4 mM MgATP, 0.3 mM Na_2-GTP, and 10 mM Na_2-Phosphocreatine, adjusted to pH 7.2, 305 mOsm. Internal solutions included 200 μM Ca^{2+} indicator Fluo-5F and 30 μM Alexa 594 for pyramidal cells, 200 μM Alexa 488 or calcein and 20 mM GABA (Bouhours et al., 2011) for interneurons. Recordings were discarded if pyramidal cells depolarized to >−50 mV or interneurons depolarized to >−43 mV (not corrected for liquid junction potentials). Hyperpolarizing currents <200 pA (pyramidal cells) or <160 pA (interneurons) were injected to keep the membrane potential steady. Series resistance was monitored throughout the experiment (20.3 ± 8.1 MΩ, mean ± SD, average SD = 2.3 MΩ) and post hoc corrected (see Supplemental Experimental Procedures).

Imaging

Two-photon imaging was accomplished with a custom-built two-photon laser-scanning microscope based on a Zeiss Axiovert 35 microscope with a 40 × 1.15-NA water-immersion objective (Olympus) and two tunable Ti-Sapphire laser (Spectra-Physics). Structural imaging was performed at 750 nm (excitation of Alexa 488 and Alexa 594) and Ca^{2+} imaging was performed at 810 nm (excitation of Fluo-5F and Alexa 594). For Ca^{2+} imaging, signals were collected during 500–800 Hz line scans across the dendrite, also covering spines visible in the imaging plane. Often two spines could be covered on either side of the shaft. If more spines were present, selection was random. Our data covered mostly mushroom and stubby spines. Ca^{2+} signals were quantified as increase in green fluorescence from baseline, normalized to the average red fluorescence ($\Delta Ca^{2+} = \Delta G/R$). Ca^{2+} inhibition was calculated as average ($1 - \Delta Ca^{2+}_{inh}/\Delta Ca^{2+}_{ctrl}$) from a minimum of five inhibited (+) and six uninhibited (−) sweeps (−+−+−+−+−+−) by averaging the two inhibition values obtained from the (+−) and the (−+) series.

Data Analysis

Acquisition and online analysis of imaging data were performed using custom software written in LabVIEW (National Instruments). Acquisition of electrophysiology data was performed using pClamp 10.3 (Molecular Devices). Offline analysis of imaging and electrophysiology data was performed using custom routines written in MATLAB (The MathWorks).

Statistics

To detect statistically significant inhibition in an unbiased approach, we performed the non-parametric sign-test on the full Ca^{2+}-inhibition dataset of all stimulations between ±15 μm distance and ±15 ms spike-timing delay, calculated based on ΔCa^{2+} integrated over 100 ms (Bonferroni-Holm correction was applied for different stimulation protocols). The significant absence of inhibition was inferred by a one-tailed sign-test with 0.05 upper bound. In Figure 8, spike-timing dependence was considered significant if the number of datasets, for which optimal spike-timing was reproducible after splitting the dataset in half, was significantly above chance levels ($p < 0.05$ with binomial test). Variance and standard error of Ca^{2+} inhibition were estimated by bootstrapping. Errors of inhibition ratios were estimated by error propagation.

See Supplemental Experimental Procedures for additional information.

SUPPLEMENTAL INFORMATION

Supplemental Information includes Supplemental Experimental Procedures, four figures, and one table and can be found with this article online at http://dx.doi.org/10.1016/j.neuron.2015.07.003.

AUTHOR CONTRIBUTIONS

C.J.W., F.E.M., and T.B. conceived the project. F.E.M. designed and conducted the experiments, data analysis, and modeling. F.E.M., C.J.W., and T.B. wrote the manuscript.

ACKNOWLEDGMENTS

We thank Mark Hübener, Idan Segev, and Volker Scheuss for comments on the manuscript and Ursula Weber, Marianne Braun, Frank Voss, Max Sperling, Volker Staiger, and Claudia Huber for technical assistance. This work was supported by the Max Planck Society, Marie Curie ERG grant 256284 (C.J.W.), and the German National Academic Foundation (F.E.M.).

Received: May 20, 2014
Revised: May 5, 2015
Accepted: July 9, 2015
Published: August 5, 2015

REFERENCES

Bar-Ilan, L., Gidon, A., and Segev, I. (2012). The role of dendritic inhibition in shaping the plasticity of excitatory synapses. Front. Neural Circuits *6*, 118.

Baroncelli, L., Braschi, C., Spolidoro, M., Begenisic, T., Maffei, L., and Sale, A. (2011). Brain plasticity and disease: a matter of inhibition. Neural Plast. *2011*, 286073.

Bartos, M., Vida, I., Frotscher, M., Geiger, J.R.P., and Jonas, P. (2001). Rapid signaling at inhibitory synapses in a dentate gyrus interneuron network. J. Neurosci. *21*, 2687–2698.

Bi, G.Q., and Poo, M.M. (1998). Synaptic modifications in cultured hippocampal neurons: dependence on spike timing, synaptic strength, and postsynaptic cell type. J. Neurosci. *18*, 10464–10472.

Bouhours, B., Trigo, F.F., and Marty, A. (2011). Somatic depolarization enhances GABA release in cerebellar interneurons via a calcium/protein kinase C pathway. J. Neurosci. *31*, 5804–5815.

Bourne, J.N., and Harris, K.M. (2011). Coordination of size and number of excitatory and inhibitory synapses results in a balanced structural plasticity along mature hippocampal CA1 dendrites during LTP. Hippocampus *21*, 354–373.

Branco, T., and Häusser, M. (2010). The single dendritic branch as a fundamental functional unit in the nervous system. Curr. Opin. Neurobiol. *20*, 494–502.

Breton, J.D., and Stuart, G.J. (2012). Somatic and dendritic GABA(B) receptors regulate neuronal excitability via different mechanisms. J. Neurophysiol. *108*, 2810–2818.

Chalifoux, J.R., and Carter, A.G. (2011). GABAB receptor modulation of voltage-sensitive calcium channels in spines and dendrites. J. Neurosci. *31*, 4221–4232.

Chen, J.L., Villa, K.L., Cha, J.W., So, P.T., Kubota, Y., and Nedivi, E. (2012). Clustered dynamics of inhibitory synapses and dendritic spines in the adult neocortex. Neuron *74*, 361–373.

Chiu, C.Q., Lur, G., Morse, T.M., Carnevale, N.T., Ellis-Davies, G.C., and Higley, M.J. (2013). Compartmentalization of GABAergic inhibition by dendritic spines. Science *340*, 759–762.

Christie, B.R., Eliot, L.S., Ito, K., Miyakawa, H., and Johnston, D. (1995). Different Ca2+ channels in soma and dendrites of hippocampal pyramidal neurons mediate spike-induced Ca2+ influx. J. Neurophysiol. *73*, 2553–2557.

Cichon, J., and Gan, W.B. (2015). Branch-specific dendritic Ca(2+) spikes cause persistent synaptic plasticity. Nature *520*, 180–185.

Cobb, S.R., Buhl, E.H., Halasy, K., Paulsen, O., and Somogyi, P. (1995). Synchronization of neuronal activity in hippocampus by individual GABAergic interneurons. Nature *378*, 75–78.

Cutsuridis, V. (2011). GABA inhibition modulates NMDA-R mediated spike timing dependent plasticity (STDP) in a biophysical model. Neural Netw. *24*, 29–42.

Gidon, A., and Segev, I. (2012). Principles governing the operation of synaptic inhibition in dendrites. Neuron *75*, 330–341.

Groen, M.R., Paulsen, O., Pérez-Garci, E., Nevian, T., Wortel, J., Dekker, M.P., Mansvelder, H.D., van Ooyen, A., and Meredith, R.M. (2014). Development of dendritic tonic GABAergic inhibition regulates excitability and plasticity in CA1 pyramidal neurons. J. Neurophysiol. *112*, 287–299.

Hao, J., Wang, X.D., Dan, Y., Poo, M.M., and Zhang, X.H. (2009). An arithmetic rule for spatial summation of excitatory and inhibitory inputs in pyramidal neurons. Proc. Natl. Acad. Sci. USA *106*, 21906–21911.

Hayama, T., Noguchi, J., Watanabe, S., Takahashi, N., Hayashi-Takagi, A., Ellis-Davies, G.C., Matsuzaki, M., and Kasai, H. (2013). GABA promotes the competitive selection of dendritic spines by controlling local Ca2+ signaling. Nat. Neurosci. *16*, 1409–1416.

Jack, J.J.B., Noble, D., and Tsien, R.W. (1975). Electric Current Flow in Excitable Cells (Oxford: Clarendon Press).

Jadi, M., Polsky, A., Schiller, J., and Mel, B.W. (2012). Location-dependent effects of inhibition on local spiking in pyramidal neuron dendrites. PLoS Comput. Biol. *8*, e1002550.

Kanemoto, Y., Matsuzaki, M., Morita, S., Hayama, T., Noguchi, J., Senda, N., Momotake, A., Arai, T., and Kasai, H. (2011). Spatial distributions of GABA receptors and local inhibition of Ca2+ transients studied with GABA uncaging in the dendrites of CA1 pyramidal neurons. PLoS ONE *6*, e22652.

Klausberger, T. (2009). GABAergic interneurons targeting dendrites of pyramidal cells in the CA1 area of the hippocampus. Eur. J. Neurosci. *30*, 947–957.

Koch, C., Poggio, T., and Torre, V. (1983). Nonlinear interactions in a dendritic tree: localization, timing, and role in information processing. Proc. Natl. Acad. Sci. USA *80*, 2799–2802.

Larkum, M.E., Zhu, J.J., and Sakmann, B. (1999). A new cellular mechanism for coupling inputs arriving at different cortical layers. Nature *398*, 338–341.

Liu, G. (2004). Local structural balance and functional interaction of excitatory and inhibitory synapses in hippocampal dendrites. Nat. Neurosci. *7*, 373–379.

López-Bendito, G., Sturgess, K., Erdélyi, F., Szabó, G., Molnár, Z., and Paulsen, O. (2004). Preferential origin and layer destination of GAD65-GFP cortical interneurons. Cereb. Cortex *14*, 1122–1133.

Losonczy, A., Makara, J.K., and Magee, J.C. (2008). Compartmentalized dendritic plasticity and input feature storage in neurons. Nature *452*, 436–441.

Lovett-Barron, M., Turi, G.F., Kaifosh, P., Lee, P.H., Bolze, F., Sun, X.H., Nicoud, J.F., Zemelman, B.V., Sternson, S.M., and Losonczy, A. (2012). Regulation of neuronal input transformations by tunable dendritic inhibition. Nat. Neurosci. *15*, 423–430, S421–423.

Lowe, G. (2002). Inhibition of backpropagating action potentials in mitral cell secondary dendrites. J. Neurophysiol. *88*, 64–85.

Mann, E.O., and Paulsen, O. (2007). Role of GABAergic inhibition in hippocampal network oscillations. Trends Neurosci. *30*, 343–349.

Marlin, J.J., and Carter, A.G. (2014). GABA-A receptor inhibition of local calcium signaling in spines and dendrites. J. Neurosci. *34*, 15898–15911.

Megías, M., Emri, Z., Freund, T.F., and Gulyás, A.I. (2001). Total number and distribution of inhibitory and excitatory synapses on hippocampal CA1 pyramidal cells. Neuroscience *102*, 527–540.

Meredith, R.M., Floyer-Lea, A.M., and Paulsen, O. (2003). Maturation of long-term potentiation induction rules in rodent hippocampus: role of GABAergic inhibition. J. Neurosci. *23*, 11142–11146.

Miles, R., Tóth, K., Gulyás, A.I., Hájos, N., and Freund, T.F. (1996). Differences between somatic and dendritic inhibition in the hippocampus. Neuron *16*, 815–823.

Miyoshi, G., Hjerling-Leffler, J., Karayannis, T., Sousa, V.H., Butt, S.J., Battiste, J., Johnson, J.E., Machold, R.P., and Fishell, G. (2010). Genetic fate mapping reveals that the caudal ganglionic eminence produces a large and diverse population of superficial cortical interneurons. J. Neurosci. *30*, 1582–1594.

Müller, C., Beck, H., Coulter, D., and Remy, S. (2012). Inhibitory control of linear and supralinear dendritic excitation in CA1 pyramidal neurons. Neuron *75*, 851–864.

Murayama, M., Pérez-Garci, E., Nevian, T., Bock, T., Senn, W., and Larkum, M.E. (2009). Dendritic encoding of sensory stimuli controlled by deep cortical interneurons. Nature *457*, 1137–1141.

Nevian, T., and Sakmann, B. (2006). Spine Ca2+ signaling in spike-timing-dependent plasticity. J. Neurosci. *26*, 11001–11013.

Nishiyama, M., Togashi, K., Aihara, T., and Hong, K. (2010). GABAergic activities control spike timing- and frequency-dependent long-term depression at hippocampal excitatory synapses. Front. Synaptic Neurosci *2*, 22.

Park, S., and Kwag, J. (2012). Dendritic-targeting interneuron controls spike timing of hippocampal CA1 pyramidal neuron via activation of I(h). Neurosci. Lett. *523*, 9–14.

Pérez-Garci, E., Gassmann, M., Bettler, B., and Larkum, M.E. (2006). The GABAB1b isoform mediates long-lasting inhibition of dendritic Ca2+ spikes in layer 5 somatosensory pyramidal neurons. Neuron *50*, 603–616.

Pérez-Garci, E., Larkum, M.E., and Nevian, T. (2013). Inhibition of dendritic Ca2+ spikes by GABAB receptors in cortical pyramidal neurons is mediated by a direct Gi/o-β-subunit interaction with Cav1 channels. J. Physiol. *591*, 1599–1612.

Poirazi, P., Brannon, T., and Mel, B.W. (2003). Arithmetic of subthreshold synaptic summation in a model CA1 pyramidal cell. Neuron *37*, 977–987.

Pouille, F., and Scanziani, M. (2001). Enforcement of temporal fidelity in pyramidal cells by somatic feed-forward inhibition. Science *293*, 1159–1163.

Qian, N., and Sejnowski, T.J. (1990). When is an inhibitory synapse effective? Proc. Natl. Acad. Sci. USA *87*, 8145–8149.

Royer, S., Zemelman, B.V., Losonczy, A., Kim, J., Chance, F., Magee, J.C., and Buzsáki, G. (2012). Control of timing, rate and bursts of hippocampal place cells by dendritic and somatic inhibition. Nat. Neurosci. *15*, 769–775.

Sabatini, B.L., and Svoboda, K. (2000). Analysis of calcium channels in single spines using optical fluctuation analysis. Nature *408*, 589–593.

Segev, I., and Parnas, I. (1983). Synaptic integration mechanisms. Theoretical and experimental investigation of temporal postsynaptic interactions between excitatory and inhibitory inputs. Biophys. J. *41*, 41–50.

Shapley, R., Hawken, M., and Ringach, D.L. (2003). Dynamics of orientation selectivity in the primary visual cortex and the importance of cortical inhibition. Neuron *38*, 689–699.

Stokes, C.C., Teeter, C.M., and Isaacson, J.S. (2014). Single dendrite-targeting interneurons generate branch-specific inhibition. Front. Neural Circuits *8*, 139.

Stoppini, L., Buchs, P.A., and Muller, D. (1991). A simple method for organotypic cultures of nervous tissue. J. Neurosci. Methods *37*, 173–182.

Stuart, G.J., and Häusser, M. (2001). Dendritic coincidence detection of EPSPs and action potentials. Nat. Neurosci. *4*, 63–71.

Svoboda, K., Tank, D.W., and Denk, W. (1996). Direct measurement of coupling between dendritic spines and shafts. Science *272*, 716–719.

Tønnesen, J., Katona, G., Rózsa, B., and Nägerl, U.V. (2014). Spine neck plasticity regulates compartmentalization of synapses. Nat. Neurosci. *17*, 678–685.

Tsubokawa, H., and Ross, W.N. (1996). IPSPs modulate spike backpropagation and associated [Ca2+]i changes in the dendrites of hippocampal CA1 pyramidal neurons. J. Neurophysiol. *76*, 2896–2906.

Tsukada, M., Aihara, T., Kobayashi, Y., and Shimazaki, H. (2005). Spatial analysis of spike-timing-dependent LTP and LTD in the CA1 area of hippocampal slices using optical imaging. Hippocampus *15*, 104–109.

van Versendaal, D., Rajendran, R., Saiepour, M.H., Klooster, J., Smit-Rigter, L., Sommeijer, J.P., De Zeeuw, C.I., Hofer, S.B., Heimel, J.A., and Levelt, C.N. (2012). Elimination of inhibitory synapses is a major component of adult ocular dominance plasticity. Neuron *74*, 374–383.

Wierenga, C.J., Müllner, F.E., Rinke, I., Keck, T., Stein, V., and Bonhoeffer, T. (2010). Molecular and electrophysiological characterization of GFP-expressing CA1 interneurons in GAD65-GFP mice. PLoS ONE *5*, e15915.